Remote Sensing Applications: Society and Environment 42 (2026) 102017

Contents lists available at ScienceDirect

Remote Sensing Applications: Society and Environment

journal homepage: www.elsevier.com/locate/rsase

Fine-scale thermal anomaly mapping in peri-urban landscapes using HotSat-1

Can Trong Nguyen

Environment Centre, Charles University, Prague, 16200, Czech Republic

ARTICLE INFO

Keywords:
HotSat-1
Urban heat island
Thermal environment
Local scale
Thermal hotspot
peri-urban
Fine-scale

ABSTRACT

Fine-scale monitoring of thermal environments is essential for assessing urban heat islands and heat-related risks at local scale. Conventional thermal sensors, such as Landsat and MODIS, provide valuable long-term records but are limited by coarse spatial resolution. HotSat-1, launched in June 2023, offers a promising opportunity to monitor detailed patterns of urban thermal environments at very high resolution (3.5 m). This study evaluates its potential by comparing its thermal anomalies, represented by standardized thermal anomaly (as known as z-score), with Landsat-based temperature data in detecting thermal anomalies and hotspots across heterogeneous landscapes. HotSat-1 reveals pronounced fine-scale thermal heterogeneity both between and within land use categories, with statistically significant differences that are often unresolved by coarser sensors. Cross-sensor comparisons show that HotSat-1 and Landsat consistently identify major thermal coolspots and hotspots (r = 0.58, p < *0001*). However, Landsat-based data exhibits reduced sensitivity to extreme and localized thermal anomalies, particularly over small, linear, and fragmented features. Due to coarser spatial resolution, Landsat tends to detect larger and more contiguous hotspot patches, thereby potentially leading to the misclassification of thermal hotspots over cooler vegetated surfaces. This research initially presents the strong potential of HotSat-1 high-resolution thermal imagery to enhance the detection of fine-scale and localized urban heat anomalies for local-scale assessments. However, further work is necessary to address uncertainties and limitations before broader applications can be fully realized.

1. Introduction

Urban areas are increasingly recognized as harsh arenas that are particularly prone to heat-related hazards due to the high concentration of impervious surfaces, reduced vegetation cover, and anthropogenic heat emissions from transportation, industrial production, and human settlements. This agglomeration results in significantly high temperatures compared to surrounding rural areas, a phenomena known as urban heat island (UHI) effect (Oke, 1982). It is commonly observed in cities worldwide, especially in rapidly developing centers and transitional peri-urban areas (Liu et al., 2022; Nguyen et al., 2023; Ullah et al., 2025a). The intensification of heat in highly populated regions exacerbates thermal discomfort, increases energy consumption for cooling demand, and elevates the risk of heat-related illnesses and mortality, especially during heatwave events (Heaviside et al., 2017; Kong et al., 2021; Li et al., 2019; Trong et al., 2024). These impacts are likely to become more far-reaching and severe with the increasing frequency and intensity of heatwave under climate change projection (IPCC, 2021a, 2021b). The heat-related vulnerability is amplified in urban slums,

E-mail address: can.nguyen@czp.cuni.cz.

https://doi.org/10.1016/j.rsase.2026.102017
Received 28 November 2025; Received in revised form 24 January 2026; Accepted 10 April 2026
Available online 10 April 2026
2352-9385/© 2026 The Author. Published by Elsevier B.V. This is an open access article under the CC BY-NC-ND license (http://creativecommons.org/licenses/by-nc-nd/4.0/).

informal/unplanned settlements, and transitional zones, as these marginalized and low-income communities often have limited adaptive capacity to heat stress (Fobi Kontor et al., 2025; Li et al., 2024; Olufadewa et al., 2025). However, they are frequently omitted from the assessments due to their small spatial scale and disturbed and heterogeneous landscapes that make them challenging to detect in climate and urban studies. Accurate monitoring of urban thermal environments is therefore critical for developing effective heat mitigation and adaptation strategies, informing urban planning decisions, and ensuring climate justice and heat equity in the face of extreme climate (Can et al., 2025).

In urban thermal environments and urban heat monitoring, remote sensing plays a key role in the consistent and synoptic observations of land surface temperature (LST), a critical parameter for estimating thermal environments and surface UHI (SUHI) intensity (de Almeida et al., 2021; Zhou et al., 2019). Although satellite-derived LST measures land surface (skin) temperature rather than near-surface air temperature and it can be affected by cloud cover, it offers significant advantages over ground-based station measurements, such as high spatial coverage, globally consistent data, long-term observations, and ease of accessibility. Several thermal remote sensing sensors are utilized for investigating thermal environments, spanning a range of spatial resolutions from coarse (GEOS-R/ABI and Himawari-8/9) to moderate (MODIS, Sentinel-3 SLSTR, VIIRS, and AVHRR), and moderate-high resolution sensors (Landsat series, ASTER, and ECOSTRESS) (Fu et al., 2024). Among them, more than 90% of recent studies have adopted Landsat and MODIS as primary data sources because of their long-term data coverage spanning over two decades (Diem et al., 2024). MODIS provides various spatial and temporal products, with the highest temporal resolution of daily observations. Meanwhile, Landsat shows its advantage in moderate-to-high spatial resolution in thermal sensing (100/30 m) compared to other currently available sensors. These datasets therefore have significantly advanced our understanding of urban thermal environments worldwide, facilitating long-term trend assessments, and enabling cross-city comparison (Diem et al., 2024; Shi et al., 2021; Zhou et al., 2019).

Despite their valuable contributions, the generally coarse resolution of traditional thermal sensors poses significant limitations for fine-scale urban thermal environment monitoring (Li et al., 2017; Zhou et al., 2019). Urban areas exhibit considerable thermal heterogeneity at microscale due to variations in land use/land cover (LULC), building materials, surface albedo, landscape disturbances, and vegetation composition (Zhao et al., 2014). The mixed-pixel effect in coarse-resolution data often causes thermal averaging across different surface types, obscuring small-scale thermal variations, and reducing the accuracy of localized heat-risk assessments. This limitation is particularly important for detecting small-scale and narrow linear features, such as road and railway tracks, small-fragmented residential areas, and microclimate impacts of urban design interventions, which are essential for targeted heat mitigation strategies (Ahmad and Eisma, 2023; Hsieh et al., 2023).

To address these current limitations in spatial resolution, advancements in high-resolution thermal remote sensing have emerged to better facilitate fine-scale thermal environment monitoring in urban regions. Unmanned Aerial Vehicle (UAV)-based thermal imaging can actively observe at very high resolution up to centimeter-level data (Ahmad and Eisma, 2023). It can provide strong evidence to explore detailed aspects of urban thermal environments, such as temperature variations across LULC categories, micro-urban heat

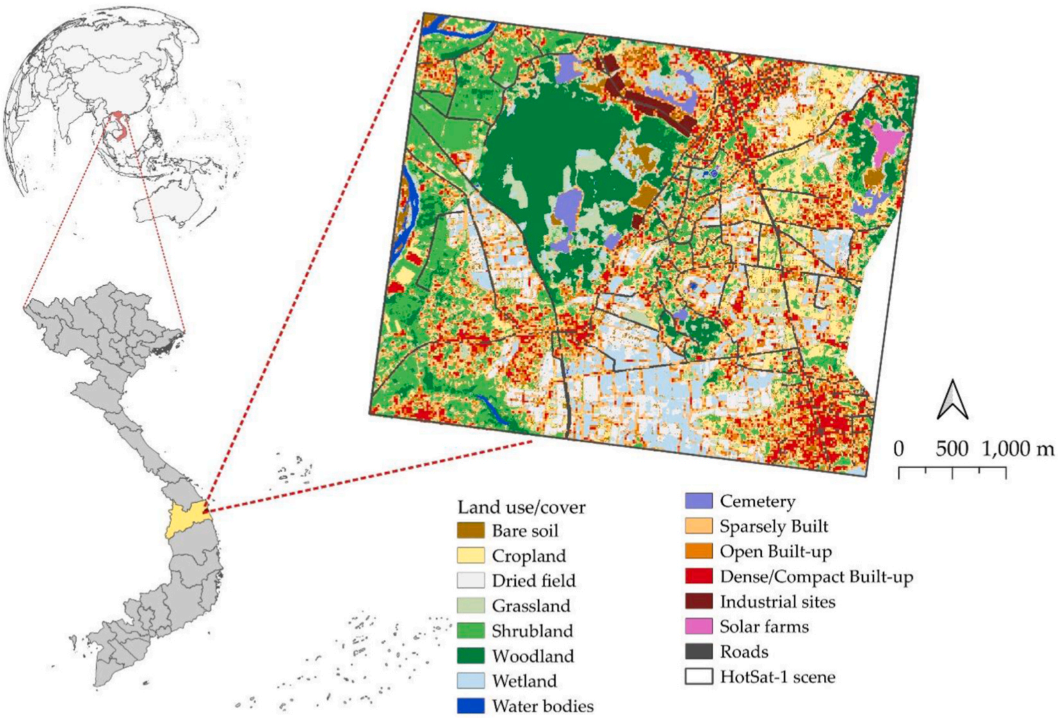

Fig. 1. Location of pilot study site in Quang Ngai province, Vietnam, showing the HotSat-1 image scene footprint and land use/land cover map. Land use and land cover map was classified from Planet NICFI imagery using random forest classifier in September 2023.

islands, thermal runoff pollution, cooling effects from urban parks and green patches, and evaluation of heat mitigation strategies (Ahmad et al., 2025; Feng et al., 2020; Li et al., 2024; Naughton and McDonald, 2019; Son and Kim, 2025). However, it remains limited in spatial coverage and temporal consistency for city-wide assessments. The recent launch of HotSat-1 in June 2023, operated by Global Satellite Vu Ltd. (SatVu), represents a promising advancement in thermal remote sensing that provides thermal infrared data at an unprecedented spatial resolution of approximately 3.5 m (SatVu, 2024). HotSat-1 has a potential to revolutionize urban thermal monitoring and research by enabling the global consistent detection of fine-scale thermal anomalies across urban landscapes, capturing heat leakage from industry and infrastructure, monitoring micro-scale heat variabilities, and improving precision of SUHI assessments in smaller communities (Holtan et al., 2025; Lin et al., 2024; Zhang et al., 2024). Although there was the technical anomaly in December 2023 resulting in the cessation of data production, it paves a potential way for a planned constellation of seven thermometer satellites for consistent monitoring with multiple revisits per day.

Despite the promising potential of HotSat-1, current evaluations of HotSat-1 capabilities for urban thermal environment remain limited. Therefore, this pilot case study evaluates the potential of HotSat-1 for fine-scale mapping of thermal environment across different LULC categories within disturbed peri-urban landscapes. A comparison with Landsat-based LST was also implemented to assess the relative performance of HotSat-1 in capturing fine-scale thermal patterns. This is one of the first efforts to inform the applicability of HotSat-1 for fine-scale thermal assessment to capture localized heat impacts. It also provides critical evident-based support for the planned SatVu constellation, which has the potential to open a new era in urban thermal research by enabling consistent, high-resolution thermal monitoring and transforming current practice in the field.

2. Methodology

2.1. Pilot study site

The pilot study site covers approximately 16 km^2, spanning from 15°1′N, 108°50′E to 14°58′N, 108°52E, which is located in Duc Hiep, Mo Duc district, Quang Ngai province, Vietnam (Fig. 1). Mo Duc lies along the South-Central Coast, about 25 km south of the city center. The region is prone to multiple natural hazards that have resulted in substantial economic losses, including not only typhoons and flooding but also temperature extremes (Duy et al., 2021). For example, it has witnessed a 2 °C increase in annual temperature over the last two decades (Pham and Saizen, 2023). The annual average temperature in the region is about 22.6 °C, with the highest temperature occurring in July (~36.3 °C). However, the temperature difference between the hottest and coldest months is nearly twofold, increasing the vulnerability of local communities to temperature extremes (Lam et al., 2024).

According to the People's Committee of Quang Ngai (PCQN), Mo Duc is oriented to become one of the province's 18 urban centers. It is an integrated urban area comprising three subregions, with a development focus on agriculture, construction, industry, commerce, and tourism (PCQN, 2022). Specifically, the district hosts three type V urban centers and four industrial clusters, with total built-up areas estimated to reach approximately 760 ha in 2030. However, the district also prioritizes forestry and centralized agriculture in the western region. As one of the region with the highest solar radiation intensity, a 24 ha solar farm with capacity of 19.2 MW was established in the district in 2015 (Da et al., 2016). These diverse development orientations have led to a highly fragmented landscapes, potentially rising localized thermal heterogeneity that may disproportionately affect indigenous communities.

2.2. Datasets and preprocessing procedures

2.2.1. Hotsat-1 thermal Level-2 data

HotSat-1, the first satellite in the planned constellation initiated by Global Satellite Vu Ltd. (SatVu), was launched in June 2023 and remained operational until December 2023 (SatVu, 2024). The satellite is designed to monitor heat variations from industrial and infrastructure sources, supporting analyses of heat-related phenomena, energy efficiency, and environmental and climate change accountability.

The HotSat-1 is a Mid-wave Infrared (MWIR) imaging sensor capable of operating in two modes for nighttime (3700 – 4950 nm) and daytime (4325– 4950 nm) observations, with a sensitivity of approximately 2 K (SatVu, 2024). The sensor is carried on a microsatellite platform (~130 kg) operating in a Sun-synchronous obit at an altitude of approximately 500 km. It captures images with a swath size of 4.5 × 3.5 km at a spatial resolution from 3.5 to 6.8 m, depending on the viewing angle (SatVu, 2023).

The raw data of HotSat is acquired by "snap video" mode, which captures 25 frames per second to offer diverse data levels (3 levels) and analysis capabilities (SatVu, 2024). The HotSat-1 used in this study is Thermal Level 2 Visual (L2). The thermal Level 1 primary (L1) data is obtained from raw frames after passing through sensor and radiometric correction. The thermal L1 data is further processed by orthorectification and radiometric enhancement—including non-uniformity correction, flat field correction, bad pixel detection and correction, frame stacking, and upsampling—to generate the thermal level-2 data. The Level-2 data offers a single orthorectified image that is stacked into a single image using the median pixel value to reduce noise (SatVu, 2024).

The HotSat-1 scene in this study was captured on 30 September 2023 at 06:11:10 (UTC) or 13:11 local time (GMT+7), with approximately 10% cloud cover. The acquired data is thermal level-2 Digital Numbers (DNs), encoded in 14-bit format at ~3.75 m resolution, providing an optimized data product for immediate interpretation and analysis (SatVu, 2025). A useable data mask (UDM) identifying bad pixels, cloud cover, saturated pixels, and areas with no data is also provided to mask out low quality pixels from further analyses.

2.2.2. Landsat 9 and MODIS daily land surface temperature

Land surface temperature observations from Landsat 9 and Moderate Resolution Imaging Spectroradiometer (MODIS) were also leveraged through spatiotemporal fusion approach to obtain LST data corresponding to the HotSat-1 acquired date for cross-comparison purposes.

Landsat 9 surface reflectance data is Level 2 that provides top-of-atmosphere reflectance data corrected for atmospheric effects, delivering surface-level reflectance values for each data band and brightness temperature (BT, °K) from thermal infrared band (TIR, 10.60–11.19 μm). With a spatial resolution of 30 m, Landsat 9 offers essential information on spectral reflectance and LST for cross-comparison with HotSat-1 observations. Yet, its revisit cycle is relatively long, at about 16 days, making the same-day observation for direct comparison unavailable. To overcome this limitation, we acquired three cloud-free Landsat 9 scenes on 05 April 2023, 10 July 2023, and 27 August 2023, with low cloud cover ratio in the study area, for data fusion with coarser data from MODIS to generate finer-scale LST reference data for 30 September 2023. The scene captured on 10 July 2023 was used for validating the data fusion approach. These Landsat scenes at path 124 and row 049 were downloaded from the USGS Explorer data archive (https://earthexplorer.usgs.gov). These scenes were preprocessed through a comprehensive workflow, including data scaling, spatial clipping, and LST estimation. More explicitly, LST used in further steps was estimated from brightness temperature (BT) after calibrating land surface emissivity, which was retrieved using an NDVI-based conversion equations (Nguyen et al., 2022).

In addition to Landsat LST data, we also acquired daily LST data from MODIS (Moderate Resolution Imaging Spectroradiometer) sensor onboard Terra and Aqua satellites. Specifically, we used the daytime MYD11A1 version 6.1 LST product from the Aqua-MODIS sensor, which captures data at 13:30 local time to better align with the HotSat-1 observation. MYD11A1 is a daily Level 3 dataset that provides emissivity and LST for both daytime and nighttime observations at an approximate spatial resolution of 1 km. Although MYD11A1 data is much coarser than Landsat and HotSat-1 data, it provides essential daily reference for cross-comparison when higher-resolution LST data sources are often unavailable at the same observation date. The MODIS daily LST data was downloaded directly from NASA's Earth Observing System Data and Information System (EOSDIS, https://search.earthdata.nasa.gov). A tile corresponding to horizontal tile 27 (h27) and vertical tile 07 (v07) was acquired for this study. Three scenes observed on the same date as Landsat observations (i.e., 05 April 2023, 10 July 2023, and 27 August 2023) were considered for LST fusion and validation. Another scene captured on 30 September 2023 was used for predicting the fine-scale Landsat-based LST using the verified fusion approach. These images were also spatially cropped and scaled to derive surface temperature values.

2.2.3. Planet NICFI image

The satellite data of PlanetScope (Planet-NICFI) provides monthly composite of surface reflectance and orthorectified mosaics data over tropical regions. It is accessed via Google Earth Engine platform (GEE) through NICFI satellite data program basemaps for tropical forest monitoring in Asia for non-commercial use (Pandey et al., 2023). It offers data at ~4.77 m resolution with four spectral bands (i.e., blue, green, red, and near-infrared), enabling detailed assessments on vegetation types discrimination, land us/cover changes, and forest loss (Trong et al., 2025; Zhang et al., 2023). We acquired a cloud-free mosaic image in September 2023, applied preprocessing steps directly on GEE and exported data for land use/land cover classification at finer pixel size.

2.3. Land use/land cover classification

A high-resolution land use/land cover (LULC) map was used as a basis for LST and urban heat island comparisons across LULC categories and sensors. This high-resolution LULC map was classified from Planet-NICFI data at approximately 5-m resolution using a random forest supervised classifier. In addition to the four original bands from Planet, we derived several spectral indices to capture diverse spectral characteristics of LULC features, including VARI (Visible Atmospherically Resistant Index), GLI (Green Leaf Index), EVI (Enhanced Vegetation Index), LAI (Leaf Area Index), GDVI (Generalized Difference Vegetation Index), Modified Bare soil Index (MBI), and NLI (Nonlinear Vegetation Index) (Can et al., 2021; Goel and Qin, 1994; Huete et al., 1997; Louhaichi et al., 2001; Montero et al., 2023; Wu, 2014). Reference ground truth points were manually generated based on visual interpretation and very-high-resolution Google Earth images. The reference data was divided into two independent datasets, with 70% used for training and 30% for validating the classification algorithm. A random forest classifier was trained on the training dataset, using the number of trees (*ntree*) set to 500 to ensure the model stability and prevent overfitting, which achieved an overall accuracy of 98.02% (*kappa* = 0.976). The initial LULC generated from this machine learning-based identified diverse LULC categories, such as sandy barren, fallow field, mixed built-up, dense built-up, road, solar farm, grassland, shrubland, cropland, forest/woodland, wetland, and water bodies. To accurately capture the detailed and heterogeneous landscapes within the pilot site, the initial LULC map was refined using very-high-resolution Google Earth imagery and Open Street Map (OSM) to discriminate roads, industrial sites, and cemeteries. A subsequent step utilized built-up surface fraction (BSF) to further classify built-up areas into sparsely built-up ($0.2 < BSF < 0.4$), open built-up ($0.4 < BSF < 0.6$), and dense/compact built-up categories ($BSF > 0.6$), to better capture local climate characteristics (Wang et al., 2025). The output LULC map is able to describe landscape heterogeneities through 15 categories, including bare soil (BS), cropland (CRP), shrubland (SH), grassland (GL), forest/woodland (WL), water bodies (WAT), roads (RD), solar farms (SF), wetland (WET), dried/fallow field (DF), industrial sites (IN), cemetery (CEM), sparsely built-up (SBU), open built-up (OBU), and dense/compact built-up (CBU) (Fig. 1).

2.4. Landsat-MODIS LST fusion

A fusion approach between Landsat 9 and MODIS daily LST data was implemented to leverage the detailed spatial information from

Landsat and high temporal resolution of MODIS, enabling the generation of fine-scale LST for the target date corresponding to HotSat-1 observation when Landsat 9 data was unavailable. We have adopted the enhanced spatial and temporal adaptive reflectance fusion model (ESTARFM), developed based on the STARFM algorithm, to simulate and predict fine-scale LST on 30 September 2023 based on coarse resolution daytime LST from MYD11A1 data on the same date (Diem et al., 2022; Zhu et al., 2010). More specifically, LST of MODIS and Landsat derived from initial preprocessing steps in Section 2.2.2 were further prepared before being input into the ESTARFM data fusion model. It requires two pairs of coarse and fine references at the same time and one coarse image at the target time to simulate and predict the high resolution LST data. Two pairs of reference images are analyzed both spatial and temporal information by the algorithm. More explicitly, ESTARFM uses a moving window to identify spectrally and thermally similar pixels, with adaptive weights based on temporal changes and spatial patterns to improve fusion accuracy in heterogeneous landscapes (Zhu et al., 2010). Subsequently, these relationships between LST changes across sensors are leveraged to predict the corresponding LST at the prediction time while accounting for local heterogeneities within the considered area.

Prior to the fusion step, Landsat 9 and MYD11A1 LST images were clipped to the considered area in Fig. 1. Individual MODIS images were resampled to match the number of rows and columns of the Landsat data. A bilinear resampling method was applied to reduce the effects of geo-referencing errors. Geo-rectification was also performed to ensure that the MODIS and Landsat image pairs absolutely were precisely aligned in spatial extent. The temperature values from Landsat and MODIS LST were scaled and transformed to 16-bit signed integer (int16) to enhance the sensitivity and computational efficiency of the algorithm.

The simulated LST on 10 July 2023 was validated using Landsat-derived LST acquired on the same date to evaluate the effectiveness of data fusion under local conditions for further predictions in the target date. The fusion model performed well, achieving a balanced result with a correlation coefficient of $r = 0.894$ (95% CI: 0.892 – 0.897, $p < 0.001$; Supplementary Figs. S1–2) and a mean absolute error (MAE) of 1.716 °C. Subsequently, these paired datasets were utilized to predict fine-grained LST for 30 September 2023.

2.5. Analytical procedures

Since the HotSat-1 thermal Level-2 data offers DN values rather than direct surface temperature measurement, and no algorithm is currently available to convert thermal Level-2 data to real surface temperature, we therefore applied standardized thermal anomaly (STA, as known as the z-score, Eq. (1)) (Nabizada et al., 2022) for relative thermal anomaly detection based on both HotSat-1 thermal data and Landsat-based LST for 30 September 2023.

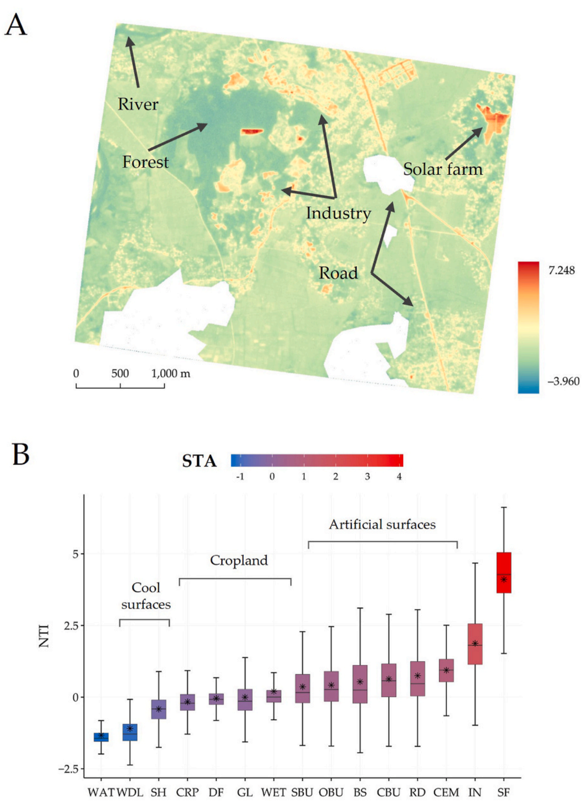

Fig. 2. Fine-scale thermal anomalies measured by HotSat-1. (A) STA image showing the dynamic value range of thermal values across cool and hot surfaces, and (B) boxplot of STA values for different land use and land cover categories, with the middle points in representing mean values.

$$STA = \frac{T_i - \mu}{\sigma} \tag{1}$$

where Ti is thermal signals at pixel i, which can be LST from Landsat or thermal DN values; μ is the mean value of thermal signals across the entire scene; and σ is the corresponding standard deviation.

It allows robust comparison of thermal heterogeneity in the absence of absolute surface temperatures. Positive STA values indicate pixels that are warmer than the scene average, whereas negative STA values present relatively cooler surfaces. STA values were calculated for each land use and land cover category, and mean values were compared among land use types using ANOVA test. Hotsat-1 and Landsat-based LST images were also georeferenced to a common coordinate system (WGS84/UTM zone 49N) using standard geometric correction procedures. To facilitate cross-sensor comparisons, given spatial differences between the two sensors and also with land use and land cover map, different spatial alignments have been performed based on analytical purposes. More explicitly, the spatial correction between HotSat-1 and Landsat-based STA was analyzed using spatially aggregated HotSat-1 data to match the Landsat pixel size (30 m). For other analyses, resampling method was applied to retain the original pixel details of each dataset. To further illustrate the performance of HotSat-1 in capturing fine-scale thermal patterns, visualization of thermal anomalies along transects across diverse land use and land cover categories was also conducted. Thermal hotspots were additionally identified as areas where $Ti > \mu + 0.5 \times \sigma$. The spatial overlap of hotspots detected by both sensors, as well as areas uniquely identified by each sensor, was further analyzed to reveal spatial features in thermal patterns between the two datasets.

3. Results

To explore fine-scale thermal patterns captured by HotSat-1, we analyzed thermal anomalies and hotspot detection using standardized thermal anomaly (z-score) derived from HotSat-1 against its medium-resolution counterpart, Landsat. The evaluations focus on three aspects: (i) the ability to capture thermal heterogeneities across land cover classes, (ii) cross-sensor consistency in spatial patterns, and (iii) the detection of unique and extreme hotspot detection, to highlight the advantages of high-resolution thermal data for presenting localized thermal anomalies.

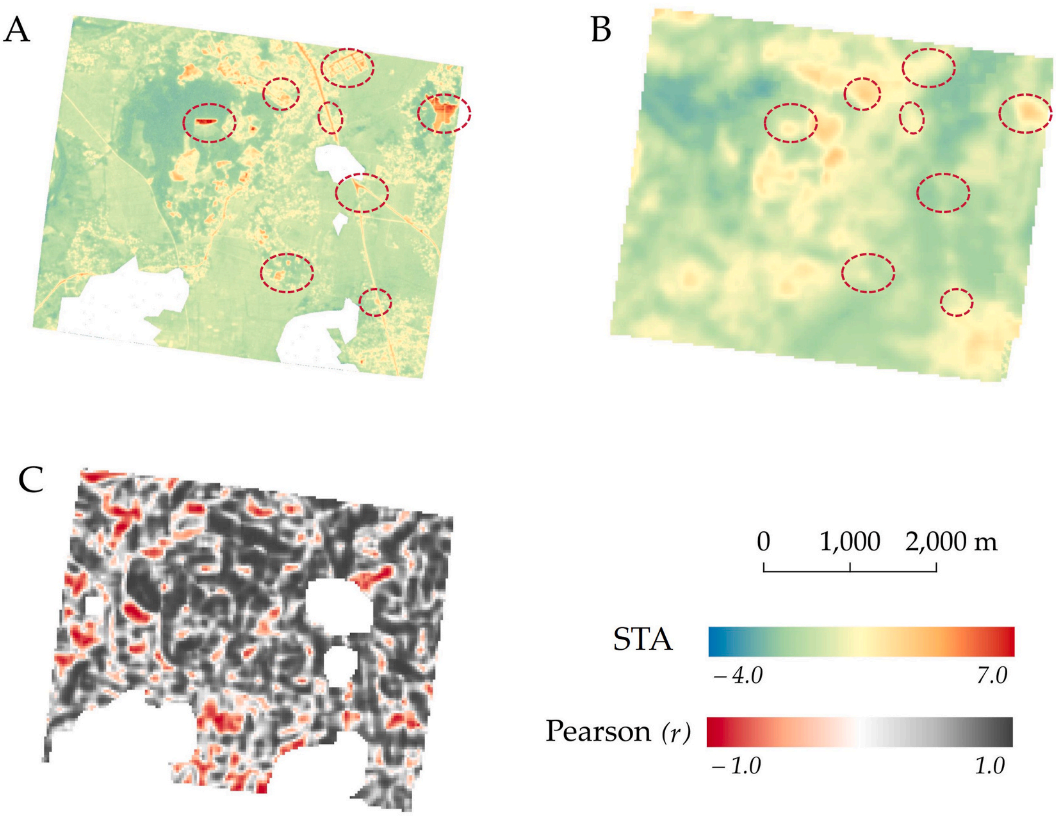

Fig. 3. Cross-comparison of STA between HotSat-1 and Landsat-based data for 30 September 2023 with dashed circles highlighting major differences. (A) STA derived from HotSat-1, (B) STA derived from Landsat-based fusion data, and (C) spatial correlation between HotSat-1 and Landsat-based STA at a comparable spatial resolution of 30 m.

3.1. Thermal heterogeneity captured by HotSat-1

Fig. 2A illustrates thermal patterns captured by high-resolution HotSat-1 imagery, represented by standardized thermal anomaly (NTI) across the pilot site. The STA is derived from L3 thermal DN values and reflects the relative thermal anomaly of each pixel, indicating whether it is hotter or cooler compared to the entire landscape. Although the STA cannot offer absolute surface temperature, it is comparatively robust for characterizing thermal heterogeneity between land use categories in the absence of a HotSat-1 calibration algorithm to convert DN values to LST. It is able to depict pronounced fine-scale thermal heterogeneity among land use categories. STA values range from approximately −4 to +7, which indicates substantial variation in relative thermal conditions. Primary hotspots and coolspots are clearly visible in the STA image. Cool surfaces, such as water bodies and woodland, exhibit negative STA values, whereas industrial areas, roads, and solar farms are highlighted by markedly positive STA values. In addition to the hotspots with extreme thermal signals, microscale thermal contrasts are also clearly observed within urban and peri-urban landscapes, manifested as thermal gradient transitioning from compact built-up areas to more sparsely urban patches.

Quantitative analysis of STA values across different land cover types further supports the thermal heterogeneity observed in HotSat-1 data (Fig. 2B and Table S1). Water surfaces and woodland consistently display the lowest STA values, with average STA values below −1, as their typical role for local cooling elements. Sparse and low vegetated landscapes, such as croplands, grasslands, and wetlands, exhibit more moderate thermal characteristics, with STA values spanning around zero. In contrast, artificial surfaces, including sparse and compact built-up areas, roads, and industrial sites, show elevated STA values, as the primary contributors to urban heat effects. Notably, HotSat-1 imagery effectively identifies pronounced thermal anomalies within artificial surface, such as industrial sites and solar farms, with STA values reaching up to 4.1. Beyond inter-class differences between land cover types, HotSat-1 is also sensitive to intra-class heterogeneity. For example, variations in thermal anomalies among sparsely vegetated land use areas or artificial surfaces, despite their similar thermal characteristics that are often difficult to distinguish using conventional satellite resolutions. Both inter-class and intra-class heterogeneities are statistically significant, as confirmed by ANOVA test ($p < 0.001$), indicating that fine-granular HotSat-1 thermal data allows for accurate detection of fine-scale thermal patterns with systematically different thermal distributions across and within land cover types.

3.2. Cross-sensor spatial correspondence of thermal anomalies

To examine cross-sensor consistency in spatial thermal patterns, we compare the variation, distribution, and spatial alignment of NTI-derived thermal anomalies observed in HotSat-1 and Landsat-based data. Both datasets can consistently identify major thermal hotspots and coolspots across the study area (Fig. 3A and B), with a high level of spatial correspondence (Fig. 3C). To account for scale effects on spatial correspondence, HotSat-1 STA is spatially aggregated to simulate and approximate the mixing of thermal signals associated with Landsat coarser pixel size. Following this aggregation, the spatial correlation between the two STA datasets increased and reached $r = 0.58$ ($p < 0.001$). Notably, the highest levels of spatial correspondence are observed over surface features with pronounced and seasonally stable thermal characteristics, including solar farms ($R^2 = 0.76$), bare soil ($R^2 = 0.52$), cemetery ($R^2 = 0.49$), industrial sites ($R^2 = 0.45$), roads ($R^2 = 0.42$), and urban built-up areas (Fig. 3C and Fig. S3). It demonstrates that HotSat-1 and Landsat-based STA have strong cross-sensor consistency in capturing the spatial organization of dominant thermal anomalies.

However, due to its coarser spatial resolution, Landsat-based STA exhibits a narrower value range (2.3 to +3.5) compared to that observed in HotSat-1, revealing a reduced thermal sensitivity to extreme thermal anomalies, especially at the fine scales. In contrast, the higher resolution of HotSat-1 enables the clear detection of pronounced thermal anomalies associated with small-scale and linear features, such as small built-up patches, transportation networks, and localized heat emissions from industrial facilities. These features are frequently difficult to resolve in Landsat-based data, especially in the peri-urban landscapes, where coarser pixels and thermal mixing effects can attenuate or obscure these localized thermal signals (Fig. 3A and B). Moreover, HotSat-1 demonstrates a strong

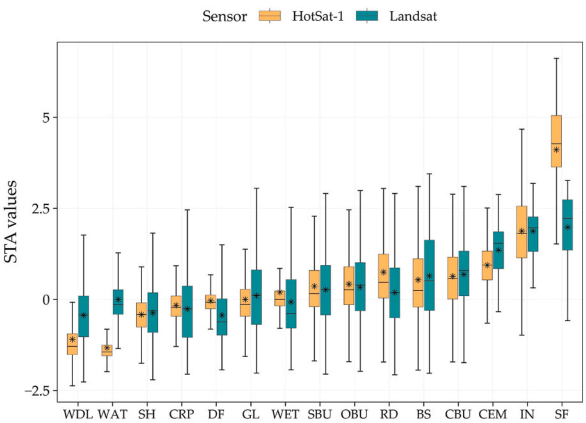

Fig. 4. Boxplot showing STA differences across land use and land cover classes for both HotSat-1 and Landsat sensors, with the middle points in representing mean values.

ability to highlight hierarchical thermal differences among land use categories, capturing both inter-class and intra class variability. While Landsat-derived STA can also be able to identify the general thermal hierarchy from cooler to warmer surfaces, its discriminatory power is comparatively weaker, particularly for land cover types with similar thermal characteristics. These include solar farms and industrial sites, a group of artificial surfaces (e.g., open and sparsely built-up areas, and roads), as well as bare soil and compact built-up areas, or other cooler surfaces such as wetland, water bodies, and croplands. Differences among these categories are not statistically significant in the Landsat data, as indicated by the ANOVA test (Fig. 4 and Table S1). This contrast is most evident for land cover types such as solar farms, woodland, and water bodies, where the STA values derived from the two sensors differ significantly (Fig. 4). This sensor-dependent divergence implies that surfaces with strong thermal inertia or pronounced sub-pixel heterogeneity are particularly sensitive to spatial resolution and signal mixing effects, which can substantially influence the interpretation of thermal anomalies using conventional thermal sensors.

This difference in thermal sensitivity is further illustrated by the transect profiles across two representative sections through diverse land cover types (Fig. 5). HotSat-1 captures sharper and more pronounced peaks of thermal anomalies corresponding to fine-scale features such as solar farms, roads, industrial sites, whereas Landsat-based STA shows smoother transitions and lower amplitude due to its coarser spatial resolution and possible pixel mixing effects. These transects emphasize how high-resolution thermal data can disaggregate or refine localized or obscured in medium-resolution datasets, particularly in peri-urban landscapes.

Comparison of thermal hotspots both sensors effectively detect the major hotspots along urban-rural gradients (Fig. 6A). The areas of overlap between the two sensors account for 48% of the total hotspot detected by Landsat, whereas HotSat-1 achieves a higher spatial agreement, covering approximately 66% of the total hotspot areas. High spatial agreement is widely observed across compact built-up areas (18.9% of overlapping areas), sparsely urban areas (17%), and open built-up areas (14.8%). Although both sensors exhibit relatively high consistency in identifying thermal hotspots, their differing spatial resolutions lead to distinct hotspot patterns. Landsat tends to detect larger and more contiguous hotspot patches along common hotspots edges, while HotSat-1 captures smaller and more scattered hotspots, particularly along urban fringes and road networks.

Among hotspot areas only detected by Landsat, there is a large proportion of hotspots distributed over grassland (13%), woodland (12.6%), shrubland (10.6%), and cropland (10.6%), which are generally cooler vegetated surface (Fig. 6B). These patterns may reflect limitations in Landsat's ability to resolve fine-scale thermal heterogeneity. Conversely, hotspots detected exclusively by HotSat-1 are predominately distributed in sparsely built-up areas (17.3%), roads (17.2%), open built-up areas (15.3%), and compact built-up areas (11.9%), suggesting that HotSat-1 finer spatial resolution can capture localized thermal variabilities and hotspots that are typically averaged out in coarser resolution Landsat thermal bands.

4. Discussions

HotSat-1 thermal data demonstrated promising potential for detailed thermal mapping over diverse and heterogeneous landscapes (15 land use/land cover types) across urban-rural settings. Clear differentiations of thermal anomalies observed among land use/land cover classes, as evidenced by statistical significance of NTI, emphasizing HotSat-1 capability to discriminate thermal signals of diverse surfaces against Landsat moderate thermal data. HotSat-1 is also sensitive to varying surface thermal properties at finer pixel size. Lower thermal anomalies (NTI) recorded in woodland, water bodies, and shrubland, higher values in impervious surfaces (e.g., built-up areas, roads, industrial sites, and solar farms) that are consistent with the inherent thermophysical characteristics of these surfaces. Moreover, HotSat-1 thermal anomaly map can capture finer thermal details at microscale thermal contrasts, including intra-urban variability among different types of built-up types and linear heat signatures along road networks, which are frequently smoothed

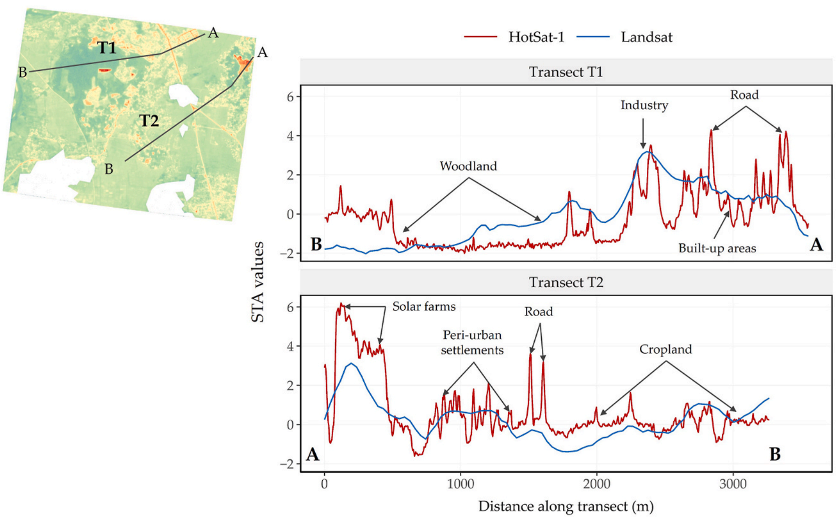

Fig. 5. Thermal anomalies and differences between HotSat-1 and Landsat along transects across over different land use and land cover categories.

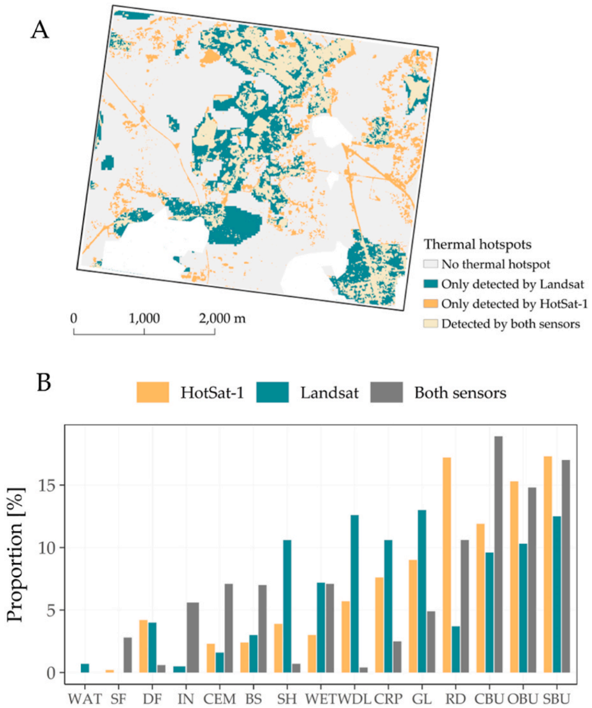

Fig. 6. Hotspots detection by HotSat-1 and Landsat-based data. (A) Discrepancies in spatial detection of thermal hotspots in HotsSat-1 and Landsat data, and (B) proportion of land use and land cover types within hotspot areas.

out and obscured in coarser-resolution datasets. This enhanced spatial resolution enables better identification of microscale thermal hotspots for localized mitigation planning.

The generally higher thermal anomalies (NTI) values recorded by HotSat-1, particularly over solar farms, industrial sites, roads, and compact built-up areas, reveals that coarse-resolution sensors like Landsat may fail to fully capture the magnitude of thermal peaks and extreme surface temperatures in important thermal hotspots. It underscores the importance of selecting high-resolution thermal sensors for urban heat studies, especially in local scale investigations with spatially fragmented landscapes along urban-rural gradients to ensure accurate representation of heat and impacts. It is particularly meaningful for assessing heat leakage and thermal pollution, as it helps to uncover localized impacts of industrial sites, infrastructure projects, and solar farms on nearby ecosystems and indigenous communities. It also highlights the potential for HotSat-1 data to provide more accurate and spatially detailed thermal information.

High resolution of HotSat-1 excludes spurious thermal hotspot detection in typically cool surfaces (e.g., shrubland and woodland), which mistakenly identified by Landsat. It should be interpreted cautiously, as they may partially result from spatial averaging rather than true surface heating. Moreover, HotSat-1 effectively identifies locally remote and fragmented thermal anomaly hotspots over sparsely built-up, open built-up, and road network, underscoring its superior ability of to detect localized heat-affected zones that may be overlooked due to their small scales and fragmentation in peri-urban and disturbed landscapes. These areas, often situated in transitional zones, informal urban settlements, unplanned urban areas, and urban slums (Ullah et al., 2025b), are critical in target-oriented and inclusive heat mitigation planning because they frequently have low adaptive capacity and heightened vulnerability to heat stress. The capability of HotSat-1 to delineate these microscale thermal anomalies supports more precise identification of priority intervention areas, allowing planners to design localized cooling strategies, deploy green infrastructure, and target heat mitigation measures where they are most needed. This enhanced granularity can contribute significantly to improving the effectiveness of heat mitigation planning, particularly at the neighborhood and community scales.

However, rather than overemphasizing the advantages of high-resolution thermal data alone, it suggests that such data should be viewed as a complementary source to medium-resolution observations, which typically offer broader spatial coverage and more frequent temporal sampling. High-resolution thermal imagery primarily contributes by resolving sub-pixel thermal heterogeneity, which is critical for identifying localized hotspots that are often the focus of urban greening strategies, heat mitigation measures, and infrastructure planning. In this context, data fusion and downscaling approaches are still promising to leverage advantages of each sensor for comprehensive and spatially detailed assessments of thermal environments.

Although HotSat-1 STA uncovers valuable thermal information for thermal environment research at local scale, some uncertainties and limitations warrant consideration. No direct Landsat LST data is available for the same dates as HotSat-1 acquisitions, while MODIS-LST and Sentinel-3 LST are too coarse for single-scene analysis and comparison. The current Landsat LST used for comparison was derived from data fusion, which may introduce uncertainties due to the fusion algorithm and cross-sensors integration, especially for seasonal land use types. Also, the absence of calibration algorithms to absolute LST leads to current assessments mainly based on relative thermal anomalies of NTI. Future studies would benefit from integrating in in-situ measurements or cross-calibration with well-established LST dataset to quantify absolute surface temperatures and improve the physical interpretation of observed thermal anomalies. Additionally, the study focuses on a single scene and the temporal variability of thermal patterns urban different landscapes and meteorological conditions remain unexplored. Fure research could expand spatial and temporal coverage, integrate multi-sensors, and incorporate validation campaigns to improve both accuracy and generalizability of fine-scale thermal environment assessments.

5. Conclusion

This pilot study demonstrates the strong potential of HotSat-1 high-resolution thermal remote sensing data for investigating fine-scale spatial heterogeneities of urban thermal environments. It effectively distinguishes thermal signals across diverse landscapes with statistical significance against Landsat coarse resolution data. It can capture fine-scale and detailed patterns of both thermal anomalies, including intra-urban variabilities, thermal heat sources like industrial activities and heat leakages, and linear thermal features along road networks, surpassing the spatial limitations of Landsat data. Moreover, it provides superior capabilities to identify localized and fragmented hotspots that are often missed by coarse sensors for better targeted heat mitigation planning, especially in transitional zones and informal settlements. However, further efforts should be made including completion of absolute surface temperature retrieval algorithm and calibration with coincident in-situ measurements to improve direct temperature interpretation for applied research and heat risk assessments.

Ethical statement

This research did not involve human participants, animals, or any ethically sensitive data. Therefore, no ethical approval was required for the study.

Declaration of competing interest

The authors declare that they have no known competing financial interests or personal relationships that could have appeared to influence the work reported in this paper.

Acknowledgements

The author would like to thank the European Space Agency (ESA) and Global Satellite Vu Ltd. (SatVu) for providing HotSat-1 data under Project Start-up ID PP0102582. I also acknowledge Simon Casey and Xu Teo from SatVu for technical support with HotSat-1 data acquisition. Additionally, I thank the Norway's International Climate and Forest Initiative (NICFI) Satellite Data Program for providing access to high-resolution Planet imagery through Google Earth Engine, which was instrumental for our analysis. The author's affiliation with the Environment Centre, Charles University, is funded by the Czech Science Foundation (Grant No. 23-07984X).

Appendix A. Supplementary data

Supplementary data to this article can be found online at https://doi.org/10.1016/j.rsase.2026.102017.

Data availability

The authors are unable or have chosen not to specify which data has been used.

References

Ahmad, J., Eisma, J.A., 2023. Capturing small-scale surface temperature variation across diverse urban land uses with a small unmanned aerial vehicle. Remote Sens. 15. https://doi.org/10.3390/rs15082042.

Ahmad, J., Sajjad, M., Eisma, J., 2025. Small unmanned aerial vehicle (UAV)-based detection of seasonal micro-urban heat islands for diverse land uses. Int. J. Rem. Sens. 46, 119–147. https://doi.org/10.1080/01431161.2024.2391582.

Can, T.N., Chidthaisong, A., Diem, P.K., Huo, L.Z., 2021. A modified bare soil index to identify bare land features during agricultural fallow-period in southeast Asia using landsat 8. Land 10, 1–18. https://doi.org/10.3390/land10030231.

Can, N.T., Noszczyk, T., Iabchoon, S., 2025. Soil Textures and Urban Heat: Cooling Planning Strategies. In: *Remote Sensing for Geophysicists*. CRC Press, pp. 472–484. https://doi.org/10.1201/9781003485278-40.

Da, T. Van, Co, H.X., Cuong, D.M., Linh, D.T.H., An, D.T., Hai, L.H., 2016. Potential of solar energy exploitation for human activities in central coastal area of Vietnam. VNU J. Sci. Earth Environ. Sci. 32, 83–89.

de Almeida, C.R., Teodoro, A.C., Gonçalves, A., 2021. Study of the urban heat island (Uhi) using remote sensing data/techniques: a systematic review. Environments 8, 1–39. https://doi.org/10.3390/environments8100105.

Diem, P.K., Diem, N.K., Can, N.T., Minh, V.Q., Huong, H.T.T., Diep, N.T.H., Tao, P.C., 2022. Assessing the applicability of Fusion Landsat-MODIS data for mapping agricultural land use - a case study in An Giang Province. IOP Conf. Ser. Earth Environ. Sci. 964, 012005. https://doi.org/10.1088/1755-1315/964/1/012005.

Diem, P.K., Nguyen, C.T., Diem, N.K., Diep, N.T.H., Thao, P.T.B., Hong, T.G., Phan, T.N., 2024. Remote sensing for urban heat island research: progress, current issues, and perspectives. Remote Sens. Appl. Soc. Environ. https://doi.org/10.1016/j.rsase.2023.101081.

Duy, N.H., Fox, D., Dang, D.K., Pham, L.T., Viet Du, Q.V., Nguyen, T.H.T., Dang, T.N., Tran, V.T., Vu, P.L., Nguyen, Q.H., Nguyen, T.G., Bui, Q.T., Petrisor, A.I., 2021. Predicting future urban flood risk using land change and hydraulic modeling in a river watershed in the central province of Vietnam. Remote Sens. 13, 1–24. https://doi.org/10.3390/rs13020262.

Feng, L., Tian, H., Qiao, Z., Zhao, M., Liu, Y., 2020. Detailed variations in urban surface temperatures exploration based on unmanned aerial vehicle thermography. IEEE J. Sel. Top. Appl. Earth Obs. Rem. Sens. 13, 204–216. https://doi.org/10.1109/JSTARS.2019.2954852.

Fobi Kontor, M., Brown, A., Núñez Collado, J.R., 2025. Climate justice and heat inequity in poor urban communities: the lens of transitional justice, green climate gentrification, and adaptation praxis. Urban Sci. 9, 226. https://doi.org/10.3390/urbansci9060226.

Fu, Y., Zhu, Z., Liu, L., Zhan, W., He, T., Shen, H., Zhao, J., Liu, Y., Zhang, H., Liu, Z., Xue, Y., Ao, Z., 2024. Remote sensing time series analysis: a review of data and applications. J. Remote Sens. (United States) 4, 1–33. https://doi.org/10.34133/remotesensing.0285.

Goel, N.S., Qin, W., 1994. Influences of canopy architecture on relationships between various vegetation indices and LAI and Fpar: a computer simulation. Remote Sens. Rev. 10, 309–347. https://doi.org/10.1080/02757259409532252.

Heaviside, C., Macintyre, H., Vardoulakis, S., 2017. The urban heat island: implications for health in a changing environment. Curr. Environ. Health Rep. 4, 296–305. https://doi.org/10.1007/s40572-017-0150-3.

Holtan, M.T., Clark, S.S., Conklin, D., Rajkovich, N.B., Habeeb, D., Williams, A., Aller, D., Hondula, D.M., Coseo, P., Hamstead, Z., Chester, M., 2025. Extreme heat adaptation planning: a review of evaluation, monitoring, and reporting. J. Environ. Plann. Manag. 1–26. https://doi.org/10.1080/09640568.2024.2445832, 0.

Hsieh, C.-M., Yu, C.-Y., Shao, L.-Y., 2023. Improving the local wind environment through urban design strategies in an urban renewal process to mitigate urban heat Island effects. J. Urban Plan. Dev. 149, 05023003. https://doi.org/10.1061/JUPDDM.UPENG-3923.

Huete, A.R., Liu, H.Q., Batchily, K., Leeuwen, W. Van, 1997. A comparison of vegetation indices over a global set of TM images for EOS-MODIS. Remote Sens. Environ. 59, 440–451. https://doi.org/10.1016/S0034-4257(96)00112-5.

IPCC, 2021a. Regional Fact Sheet - Urban Areas, Sixth Assessment Report (AR6).

IPCC, 2021b. Linking Global to Regional Climate Change, Climate Change 2021 – the Physical Science Basis. Intergovernmental Panel on Climate Change (IPCC). https://doi.org/10.1017/9781009157896.012.

Kong, J., Zhao, Y., Carmeliet, J., Lei, C., 2021. Urban heat island and its interaction with heatwaves: a review of studies on mesoscale. Sustainability 13. https://doi.org/10.3390/su131910923.

Lam, P.T., Tinh, P.H., Isaac-Lam, M.F., Dien, N.T., 2024. Economic losses and damages in aquaculture production caused by extreme weather events: an empirical assessment at the household scale in Quang Ngai province, Vietnam. J. Environ. Stud. Sci. https://doi.org/10.1007/s13412-024-00993-3.

Li, C., Qin, F., Liu, Z., Pan, Z., Gao, D., Han, Z., 2024. Multi-scenario assessment of landscape ecological risk in the transitional zone between the warm temperate zone and the northern subtropical zone. Front. Ecol. Evol. 12, 1–17. https://doi.org/10.3389/fevo.2024.1471164.

Li, S., Zhu, Y., Wan, H., Xiao, Q., Teng, M., Xu, W., Qiu, X., Wu, X., Wu, C., 2024. Effectiveness of potential strategies to mitigate surface urban heat island: a comprehensive investigation using high-resolution thermal observations from an unmanned aerial vehicle. Sustain. Cities Soc. 113, 105716. https://doi.org/10.1016/j.scs.2024.105716.

Li, X., Zhou, Y., Yu, S., Jia, G., Li, H., Li, W., 2019. Urban heat island impacts on building energy consumption: a review of approaches and findings. Energy 174, 407–419. https://doi.org/10.1016/j.energy.2019.02.183.

Li, Xiaoma, Zhou, Y., Asrar, G.R., Imhoff, M., Li, Xuecao, 2017. The surface urban heat island response to urban expansion: a panel analysis for the conterminous United States. Sci. Total Environ. 605–606, 426–435. https://doi.org/10.1016/j.scitotenv.2017.06.229.

Lin, M., Jin, M., Li, J., Bai, Y., 2024. GEOSatDB: global civil earth observation satellite semantic database. Big Earth Data 8, 522–539. https://doi.org/10.1080/20964471.2024.2331992.

Liu, Z., Zhan, W., Bechtel, B., Voogt, J., Lai, J., Chakraborty, T., Wang, Z.H., Li, M., Huang, F., Lee, X., 2022. Surface warming in global cities is substantially more rapid than in rural background areas. Commun. Earth Environ. 3. https://doi.org/10.1038/s43247-022-00539-x.

Louhaichi, M., Borman, M.M., Johnson, D.E., 2001. Spatially located platform and aerial photography for documentation of grazing impacts on wheat. Geocarto Int. 16, 65–70. https://doi.org/10.1080/10106040108542184.

Montero, D., Aybar, C., Mahecha, M.D., Martinuzzi, F., Söchting, M., Wieneke, S., 2023. A standardized catalogue of spectral indices to advance the use of remote sensing in Earth system research. Sci. Data 10, 1–20. https://doi.org/10.1038/s41597-023-02096-0.

Nabizada, A.F., Rousta, I., Dalvi, M., Olafsson, H., Siedliska, A., Baranowski, P., Krzyszczak, J., 2022. Spatial and temporal assessment of remotely sensed land surface temperature variability in Afghanistan during 2000–2021. Climate 10 (7), 111. https://doi.org/10.3390/cli10070111.

Naughton, J., McDonald, W., 2019. Evaluating the variability of urban land surface temperatures using drone observations. Remote Sens. 11. https://doi.org/10.3390/rs11141722.

Nguyen, C.T., Chidthaisong, A., Kaewthongrach, R., Marome, W., 2023. Urban thermal environment under urban expansion and climate change: a regional perspective from Southeast Asian big cities. In: Climate Change and Cooling Cities. Springer Nature, Singapore, pp. 151–167. https://doi.org/10.1007/978-981-99-3675-5_9.

Nguyen, C.T., Chidthaisong, A., Limsakul, A., Varnakovida, P., Ekkawatpanit, C., Diem, P.K., Diep, N.T.H., 2022. How do disparate urbanization and climate change imprint on urban thermal variations? A comparison between two dynamic cities in Southeast Asia. Sustain. Cities Soc. 82. https://doi.org/10.1016/j.scs.2022.103882.

Oke, T.R., 1982. The energetic basis of the urban heat island. Q. J. R. Meteorol. Soc. 108, 1–24. https://doi.org/10.1002/qj.49710845502.

Olufadewa, I., Abiodun, O., Oladele, R., Eze, O.I., Adeyemo, Q., Omale, J., Nnyanzi, L., Sowunmi, A., Ale, B.M., Adebiyi, A.O., Adeloye, D., 2025. Climate, health, and living condition crises in the expanding informal settlements and slums of South-West Nigeria: a case report of Ogun and Oyo states. J. Glob. Health 15, 03031. https://doi.org/10.7189/jogh.15.03031.

Pandey, P., Kington, J., Kanwar, A., Simmon, R., Abraham, L., 2023. Planet basemaps for NICFI data program - addendum to basemaps products specification. Norwegian Ministry Clim. Change.

PCQN, 2022. No. 1550/QĐ-UBND: Decision on Approving the Construction Planning Project of Mo Duc District, Quang Ngai Province (In Vietnamese).

Pham, T.L., Saizen, I., 2023. Coastal fishers' livelihood adaptations to extreme weather events: an analysis of household strategies in Quang Ngai Province, Vietnam. Humanit. Soc. Sci. Commun. 10, 1–12. https://doi.org/10.1057/s41599-023-02263-z.

SatVu, 2025. Thermal L2 Visual Imagery Product Specification. London, England.

SatVu, 2024. Imagery User Guide. London, England.

SatVu, 2023. HotSat-1 Data Sheet. London, England.

Shi, H., Xian, G., Auch, R., Gallo, K., Zhou, Q., 2021. Urban heat island and its regional impacts using remotely sensed thermal data—a review of recent developments and methodology. Land 10. https://doi.org/10.3390/land10080867.

Son, S., Kim, D., 2025. Utilizing high-resolution UAV thermal imaging for land use and land cover-based land surface temperature analysis in urban parks. Landsc. Ecol. Eng. 21, 221–233. https://doi.org/10.1007/s11355-024-00633-6.

Trong, C.N., Diem, P.K., Nghia, D.H., Diem, N.K., Diep, N.T.H., Phan, T.N., Minh, V.Q., Quang, N.H., 2025. Leveraging convolutional neural networks and textural features for tropical fruit tree species classification. Remote Sens. Appl. Soc. Environ. 39, 101633. https://doi.org/10.1016/j.rsase.2025.101633.

Trong, N.C., Nguyen, H., Sakti, A.D., 2024. Seasonal characteristics of outdoor thermal comfort and residential electricity consumption: a Snapshot in Bangkok Metropolitan Area. Remote Sens. Appl. Soc. Environ. 33, 101106. https://doi.org/10.1016/j.rsase.2023.101106.

Ullah, S., Khan, M., Qiao, X., 2025a. Evaluating the impact of urbanization patterns on LST and UHI effect in Afghanistan's cities: a machine learning approach for sustainable urban planning. In: Environment, Development and Sustainability. Springer, Netherlands. https://doi.org/10.1007/s10668-025-06249-6.

Ullah, S., Qiao, X., Tariq, A., 2025b. Impact assessment of planned and unplanned urbanization on land surface temperature in Afghaanistan using machine learning algorithms: a path toward sustainability. Sci. Rep. 15, 1–18. https://doi.org/10.1038/s41598-025-87234-x.

Wang, M., Wang, R., Ouyang, W., Tan, Z., 2025. A multi-scale mapping approach of local climate zones: a case study in Hong Kong. Urban Clim. 61, 102446. https://doi.org/10.1016/j.uclim.2025.102446.

Wu, W., 2014. The Generalized Difference Vegetation Index (GDVI) for dryland characterization. Remote Sens. 6, 1211–1233. https://doi.org/10.3390/rs6021211.

Zhang, Q., Gu, L., Jia, B., Fang, Y., 2024. Summertime compound heat extremes change and population heat exposure distribution in China. J. Clean. Prod. 485, 144381. https://doi.org/10.1016/j.jclepro.2024.144381.

Zhang, Y., Wang, X., Li, X., Du, Y., Atkinson, P.M., 2023. Monitoring monthly tropical humid forest disturbances with planet NICFI images in Cameroon. Agric. For. Meteorol. 341, 109676. https://doi.org/10.1016/j.agrformet.2023.109676.

Zhao, L., Lee, X., Smith, R.B., Oleson, K., 2014. Strong contributions of local background climate to urban heat islands. Nature 511, 216–219. https://doi.org/10.1038/nature13462.

Zhou, D., Xiao, J., Bonafoni, S., Berger, C., Deilami, K., Zhou, Y., Frolking, S., Yao, R., Qiao, Z., Sobrino, J.A., 2019. Satellite remote sensing of surface urban heat islands: progress, challenges, and perspectives. Remote Sens. 11, 1–36. https://doi.org/10.3390/rs11010048.

Zhu, X., Chen, J., Gao, F., Chen, X., Masek, J.G., 2010. An enhanced spatial and temporal adaptive reflectance fusion model for complex heterogeneous regions. Remote Sens. Environ. 114, 2610–2623. https://doi.org/10.1016/j.rse.2010.05.032.